Tidal-driven dynamics and mixing processes in a coastal ocean model with wetting and drying

Suriyan Saramul · Tal Ezer

Abstract A three-dimensional sigma coordinate numerical model with wetting and drying (WAD) and a Mellor–Yamada turbulence closure scheme has been used in an idealized island configuration to evaluate how tidally driven dynamics and mixing are affected by inundation processes. Comprehensive sensitivity experiments evaluate the influence of various factors, including tidal amplitudes (from 1- to 9-m range), model grid size (from 2 to 16 km), stratification, wind, rotation, and the impact of WAD on the mixing. The dynamics of the system involves tidally driven basin-scale waves (propagating anticlockwise in the northern hemisphere) and coastally trapped waves propagating around the island in an opposite direction. The evolutions of the surface mixed layer (SML) and the bottom boundary layer (BBL) under different forcing have been studied. With small amplitude tides, wind-driven mixing dominates and the thickness of the SML increases with time, while with large-amplitude tides, tidal mixing dominates and the thickness of the BBL increases with time. The inclusion of WAD in the simulations increases bottom stress and impacts the velocities, the coastal waves, and the mixing. However, the impact of WAD is complex and non-linear. For example, WAD reduces near-coast currents during flood but increases currents during ebb as water drains from the island back to the sea. The impacts of WAD, forcing, and model parameters on the dynamics are summarized by an analysis of the vorticity balance for the different sensitivity experiments.

Keywords Numerical modeling · Wetting and drying · Inundation · Mixing · Tides

1 Introduction

Inundation associated with changing sea level over shallow coasts and near-coast land is an important process for many coastal areas, such as lagoons, estuaries, embayments, and mudflat regions. The inundated regions may also play an important role in the interaction between the marine environment and the ecosystem (Heniche et al. 2000; Jiang and Wai 2005; Ezer et al. 2008; Sobey 2009). However, to simulate inundation processes in ocean circulation models, they must include a wetting and drying (WAD) scheme that allows the coastal boundary between water and land to move when water level changes. Such inundation models can thus be useful tools to study and possibly predict damage caused by severe events like tsunamis (e.g., Ioualalen et al. 2007) and hurricane-induced storm surges (e.g., Xie et al. 2004; Westerink et al. 2008).

A WAD scheme has been implemented recently in the Princeton ocean model (POM, Mellor 2004), hereafter WAD-POM. The scheme was tested for one- and two-dimensional cases, including hydraulic jumps,

S. Saramul (✉) · T. Ezer
Center for Coastal Physical Oceanography,
Old Dominion University, 4111 Monarch Way,
Norfolk, VA 23508, USA
e-mail: ssara002@odu.edu

dam-break problems, and a comparison with analytical solutions for non-linear long waves propagating up a sloping beach (Oey 2005, 2006). A full three-dimensional version of WAD-POM, including stratification, rivers, winds, and realistic coastlines, has been applied to Cook Inlet, Alaska, where it has successfully simulated 10-m-range high tides, mudflat flooding, and even tidal bores (Oey et al. 2007); the Cook Inlet model has also been used to simulate the movement of the Beluga whales with the tides (Ezer et al. 2008) and for comparison with remote sensing data (Ezer and Liu 2009). It should be noted that various WAD schemes have also been implemented in POM (and similar models) independently by several groups, including, for example, the three-dimensional simulation of tidal wave in San Francisco Bay (Uchiyama 2004), simulations of Japanese bays (Kamiya et al. 2006), and storm surge models (Xie et al. 2004). Our focus here is on the evaluation of the WAD-POM code developed by Oey (2005, 2006), but the results would likely apply to other WAD schemes used by finite differencing terrain-following models. Note also that inundation modeling has a longer history with finite-element and barotropic hydrodynamic models, but they will not be discussed here.

While the WAD-POM has been applied to various idealized and realistic cases, a systematic evaluation of how the WAD influences the model results is still needed. In particular, the moving coastal boundary may influence absorption of tidal energy and affect horizontal and vertical mixing processes. Oey et al. (2007) shows, for example, a change of ∼20% in the tidal amplitude and phase in Cook Inlet, when compared with a standard model without WAD. A challenging test case to evaluate the model is a channel flow with an exposed seamount (i.e., an island), a topography similar to that used in several studies with terrain-following ocean models (Beckmann and Haidvogel 1993; Mellor et al. 1998; Ezer et al. 2002); the previous studies were done without inundation (i.e., with an underwater seamount). Here, the WAD scheme allows the inundation to change the land area of the island with changes in sea level. We evaluate how the tidally driven mixing processes in shallow areas around the island are affected by inundation associated with WAD and by several factors, such as tidal amplitudes, stratification, model resolution, etc.

The paper is organized as follows: the methodology, including the model setup and the sensitivity experiments, is described in Section 2. Model results with respect to the different factors tested are discussed in Section 3, and summary and conclusions are offered in Section 4.

2 Methodology

2.1 Model setup

The model is based on the three-dimensional, primitive equations, sigma coordinates (terrain-following) POM (Mellor 2004), with the Mellor–Yamada level 2.5 turbulence closure scheme (Mellor and Yamada 1982) and WAD implementation (Oey 2005, 2006). The details of the combined WAD-POM numerical model and recent applications can be found in Oey (2005, 2006), Oey et al. (2007), Ezer et al. (2008), and Ezer and Liu (2009). An idealized exposed seamount (i.e., an island), with the maximum depth approximately 50 m, is used in this study; a mean sea level (MSL) is set to be 20 m below the maximum allowable sea level (Fig. 1). The internal (baroclinic) and external (barotropic) time steps for both WAD and without WAD (NoWAD) cases are 60 and 6 s, respectively. Note that the POM with NoWAD can use longer time steps close to the Courant–Friedrichs–Lewy (CFL) condition (Ezer et al. 2002), but for easier WAD–NoWAD comparison purposes, the smaller time step required by the stability of the WAD scheme (Oey 2005) has been used in all cases. Since the model is tested for tides as large as the 9-m range, in experiments with no WAD, the coastal boundary is represented by a vertical wall with a minimum depth of 10 m; this necessary condition, though unrealistic for shallow areas like the surf zone, is typical for many general circulation ocean models. In simulations with WAD, the minimum depth is 5 cm, whereas waters shallower than that are considered "dry" land that can become "wet" again when surface elevation rises. The horizontal rectilinear grid has a finer grid close to the seamount and a coarser grid far from the seamount (Fig. 1). The vertical sigma grid has 21 levels with higher resolution near the surface and near the bottom. A channel flow is imposed by applying open boundaries with radiation boundary conditions for baroclinic and barotropic flows at the eastern and western sides of the model domain, and closed boundaries at the northern and southern boundaries. The grid configuration (except the shallower depth) and boundary conditions are similar to those used in Mellor et al. (1998) and Ezer et al. (2002). A simple tidal forcing, starting with an ebb tide at time zero, is applied at the western boundary through sinusoidal tidal sea level and tidal velocity boundary conditions with a period of 24 h. A constant 0.2-m-s^{-1} eastward velocity is also added. A cosine zonal wind velocity field which varies with latitude (maximum westerly wind of ∼10 m s^{-1} is at the northern boundary and maximum easterly wind of ∼10 m s^{-1} is at the southern boundary) is also included

Fig. 1 The model grid, domain and bathymetry. *Top panel* shows a side view with minimum and maximum sea level and the *lower panel* shows a top view of the horizontal model grid (medium resolution case). The *blue* and the *green lines* represent the open and close boundaries, respectively. Tidal forcing (*blue arrows*) is applied at the western open boundary. The *solid white lines* are the paths used to calculate propagation signals in Fig. 4, the *horizontal black dashed line* indicates the sections shown in Figs. 6–8 and the *vertical dashed line* indicates the sections shown in Figs. 5, 12, and 13
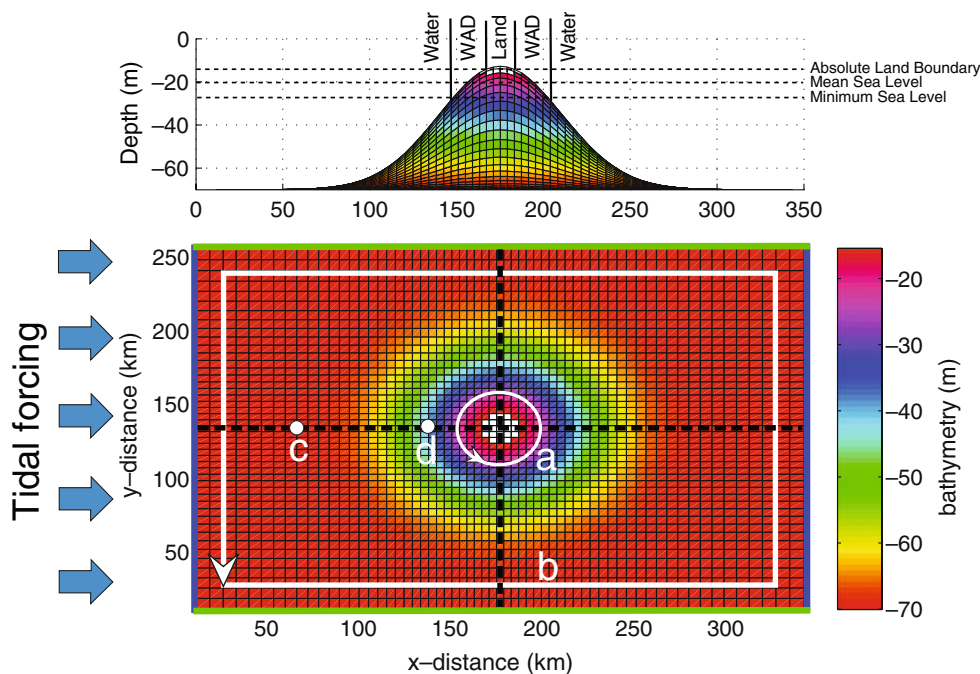
in some experiments; comparing experiments with and without winds will help to isolate the impact of wind mixing vs tidal mixing. In this study, the salinity is constant $S = 35$ psu, and the temperature decreases with depth exponentially with a maximum temperature of $\sim20°C$ at the surface and minimum temperature of $\sim10°C$ at the deepest points (some experiments are also done with no stratification). Starting from an initial condition with no horizontal variations, the model has been executed for 10 days (ten tidal cycles) with various experiments as shown in the next section. Temporal and spatial variations in stratification will develop and indicate the mixing associated with different experiments. The properties averaged over a tidal cycle will

be close to a steady state near the end of the 10-day period.

2.2 Model experiments

All the experiments are summarized in Table 1. Comparisons have been made with the model, both with WAD and NoWAD cases. For the first three experiments, we investigate the circulation pattern around the island as influenced by three different grid sizes, RS: small (2–4 km), RM: medium (4–8 km), and RL: large (8–16 km); the finest grid in each case refers to the grid size near the center of the island. Experiments TR1–TR4 aim to evaluate the impact of tidal

Table 1 The parameters used in different model experiments. Most of the experiments were repeated for both with WAD and without WAD (NoWAD)

Experiment	Grid size (horizontal cells)	Tidal range (m)	Stratification	Coriolis	Wind
RS	Small grid size: 2–4 km (131×99)	9.00 m	Yes	Yes	Yes
RM	Medium grid size: 4–8 km (65×49)	9.00 m	Yes	Yes	Yes
RL	Large grid size: 8–16 km (33×25)	9.00 m	Yes	Yes	Yes
TR1	Medium grid size	1.00 m	Yes	Yes	Yes
TR2	Medium grid size	2.75 m	Yes	Yes	Yes
TR3	Medium grid size	4.50 m	Yes	Yes	Yes
TR4	Medium grid size	9.00 m	Yes	Yes	Yes
NS1	Medium grid size	1.00 m	No	Yes	Yes
NS4	Medium grid size	9.00 m	No	Yes	Yes
NC1	Medium grid size	1.00 m	Yes	No	Yes
NC4	Medium grid size	9.00 m	Yes	No	Yes
NW1	Medium grid size	1.00 m	Yes	Yes	No
NW2	Medium grid size	2.75 m	Yes	Yes	No
NW3	Medium grid size	4.50 m	Yes	Yes	No
NW4	Medium grid size	9.00 m	Yes	Yes	No

amplitude, which might affect vertical stratification, vertical kinematic viscosity (K_M), velocity, etc. There are four different tidal ranges, TR1: 1.00 m, TR2: 2.75 m, TR3: 4.50 m, and TR4: 9.00 m, that have been tested. Two experiments, NC1 and NC4 (no Coriolis), neglects rotation, i.e., the Coriolis parameter (otherwise set to that at latitude 45°N) is set to zero. The result of this experiment might show the influence of Coriolis parameter on the pressure gradient that will be analyzed through the dynamical balance in the model compared with experiment TR1. The evolution of the surface mixed layer (SML) and bottom boundary layer (BBL) as resulted from wind-induced mixing vs tidal-induced mixing is investigated through the experiments TR1 and NW1 (with and without wind for small tidal amplitude).

In addition to qualitative comparisons between different experiments, the dynamic balance in the model will also be analyzed through the vertically integrated vorticity balance equation; see more details in Ezer and Mellor (1994, 2000). By differentiation of the two momentum equations for the vertically averaged velocity ($\bar{u}$, $\bar{v}$) and combining them, one gets the vorticity equation:

$$\frac{\partial}{\partial t}\left(\frac{\partial \bar{v}D}{\partial x} - \frac{\partial \bar{u}D}{\partial y}\right) + \frac{\partial A_y}{\partial x} - \frac{\partial A_x}{\partial y} + \frac{\partial f\bar{u}D}{\partial x} + \frac{\partial f\bar{v}D}{\partial y}$$
$$= \frac{\partial P_b}{\partial x}\frac{\partial D}{\partial y} - \frac{\partial P_b}{\partial y}\frac{\partial D}{\partial x} + \left(\frac{\partial \tau_y}{\partial x} - \frac{\partial \tau_x}{\partial y}\right)_o$$
$$- \left(\frac{\partial \tau_y}{\partial x} - \frac{\partial \tau_x}{\partial y}\right)_b, \qquad (1)$$

where f is the Coriolis parameter, $D = \eta + H$ is the water column thickness, H is the water depth relative to, say, mean sea level, η is the surface elevation, (A_x, A_y) are horizontal advection and diffusion terms, (τ_x, τ_y)$_o$ and (τ_x, τ_y)$_b$ are the surface and bottom stress, respectively, and P_b is the bottom pressure defined by

$$P_b = g\eta + \int_{-H}^{\eta} \rho g \mathrm{d}z, \qquad (2)$$

where ρ is the density and g is the gravitational constant. The equation will help us to understand the dynamic balance and evaluate the relative importance of different terms. The first term on the left represents the time-dependent "tendency" and the "A_i" terms represent advection and diffusion. Advection terms are often much larger than diffusion terms in ocean models (Ezer and Mellor 1994); this is especially true for high-resolution models like in our case, since, in the Smagorinsky diffusivity scheme used here (with a Smagorinsky coefficient of 0.1), the horizontal diffu-

sion depends on the square of the grid size. The last "f" term on the left side is the "Coriolis" term. The first terms on the right side are called the joint effect of baroclinicity and bottom relief (JEBAR, see Ezer and Mellor 1994), and as seen from Eq. 2 includes a barotropic surface slope pressure gradient term, which will be calculated separately from the baroclinic JEBAR term. The last terms represent the surface "o" and bottom "b" stress terms.

3 Model results

3.1 Basic dynamics of the flow and effect of model grid size

First, the influences of grid resolution for the 9-m tidal range case (TR4) are evaluated. Figure 2 compares surface elevation contour and surface velocity vectors for three different model grid sizes, each case for WAD and NoWAD; only the center of the model domain close to the island is shown. During high tide and the end of flood ($T = 69$ h), the vectors show the eastward-flowing tidal currents going around the island and the propagation of the tidal elevation. With WAD (Fig. 2a, c, e), the shape of the island changes with the tidal cycle by exposing/flooding land area. The model grid size also impacts the shape of the simulated island. Due to the nonlinearity (Oey 2005) and asymmetry of the flooding process (i.e., the speed of flood and ebb are different), the inundated area may be somewhat unpredictable. This grid-dependent solution is more pronounced for grids that are not parallel to the coast, while curvilinear grids and unstructured grids may provide more accurate solution near the coast as demonstrated, for example, by Chen et al. (2007). The effect of WAD on the velocity field is discussed later.

Surface elevation comparisons between WAD and NoWAD show high discrepancies, especially close to the coast (order of 20 cm in TR4). Therefore, one may ask whether this discrepancy is a constant bias or a time-dependent signal. To investigate this question, experiments TR1 (with and without WAD) are compared (TR4 discussed before shows similar results but with larger amplitudes and more noise). Figure 3 shows the surface elevation differences between WAD and NoWAD at four different times ($T = 56$ h to $T = 74$ h) related to different tidal stages. It is clearly seen that the discrepancy signal propagates clockwise around the island with a period of approximately 24 h (the period of tidal forcing at the open boundary). Positive and negative anomalies are found in opposite sides of the island with higher sea level in WAD compared to NoWAD

Fig. 2 Surface elevation (in color) and velocity vectors during high tide ($T = 69$ h) for different grid sizes (RL, RM, and RS cases from *top* to *bottom*) with WAD (*left panels*) and without WAD (*right panels*). Note that the vector scales for each case are different. The axes are in model grid numbers to indicate the different resolutions
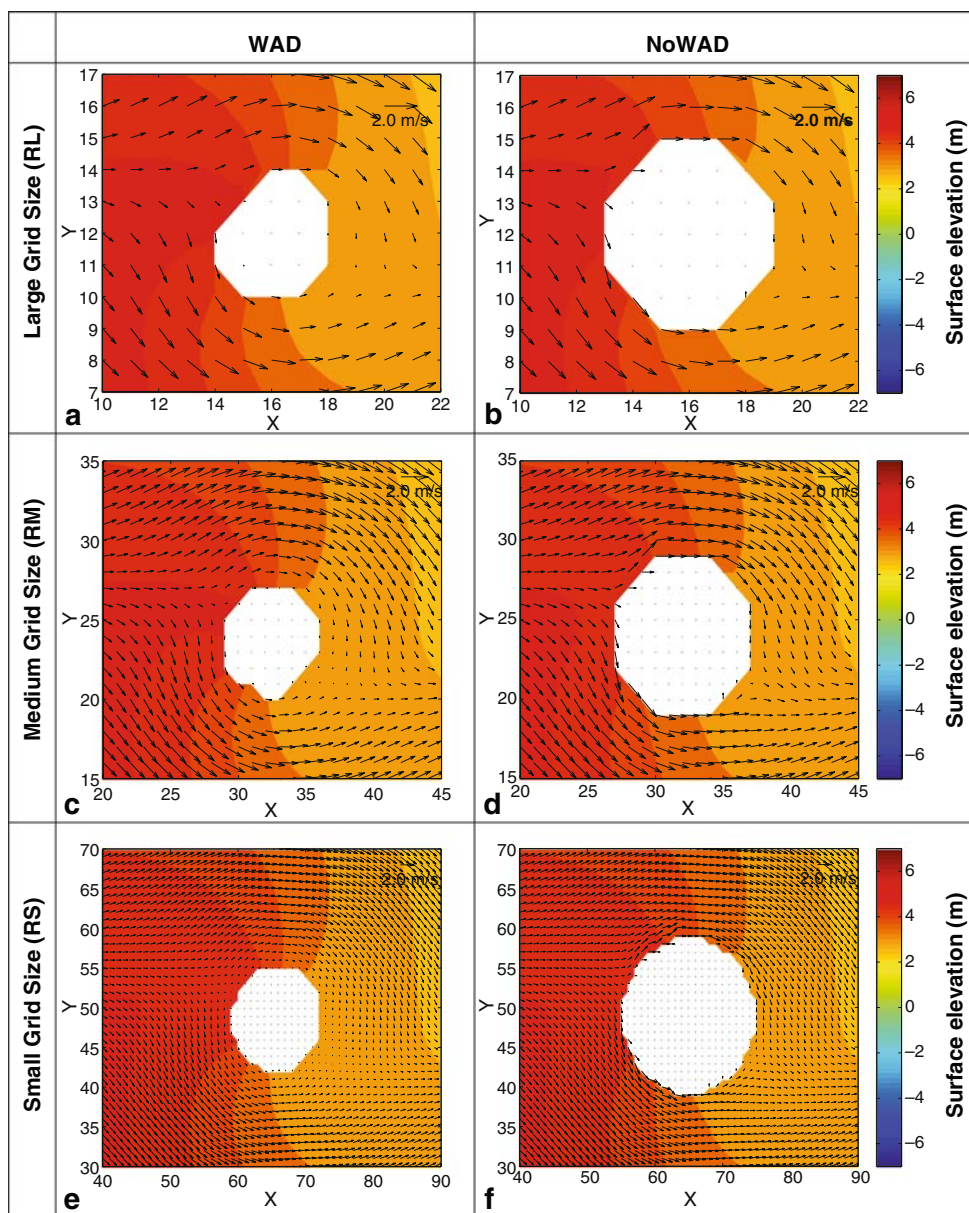

on the side of the incoming tide (e.g., during flood/ebb at $T = 62$ h/74 h flow is eastward/westward). It might be implied that the WAD impacts the clockwise propagation of topographic waves around the island as the depth is varying.

To look at the propagation of signals, the Hovmöller diagram is used in Fig. 4, plotting elevation anomaly (relative to the mean) along lines *a* (around the island) and *b* (around the model boundaries) as a function of time (see Fig. 1 for the line locations). The time axis in Fig. 4 is separated into two periods, the first few hours (bottom panels) and the first day and a half (after that, the pattern is similar for every consequential tidal cycle). Since the surface elevation is extracted in the counter-clockwise direction, the negative slope along

line *a* (white line in the left panels of Fig. 4) means a clockwise propagation; this is the direction of propagation of topographic coastal waves in the northern hemisphere, with the coast oriented to the right of the propagation direction. However, the propagation of the basin-scale waves along line *b* (right panels of Fig. 4) is counter-clockwise, i.e., in the direction opposite to the propagation of the coastal waves around the island. The propagation speed of the signal estimated from the slopes of the white lines in Fig. 4 indicates four different types of waves, with faster moving waves at the beginning of the simulation and slower waves after the initial adjustment; the propagation of the basin-scale waves is faster than that of the coastal waves. Frictionless, barotropic coastal Kelvin waves induced by

Fig. 3 The surface elevation difference (WAD minus NoWAD) for TR1 case at different times with a vector scale at the top right in each time (*top panel*). Note that the vector scale for each time is different. The *red dots* in the *lower panel* show the time of the four images with respect to the tidal cycle
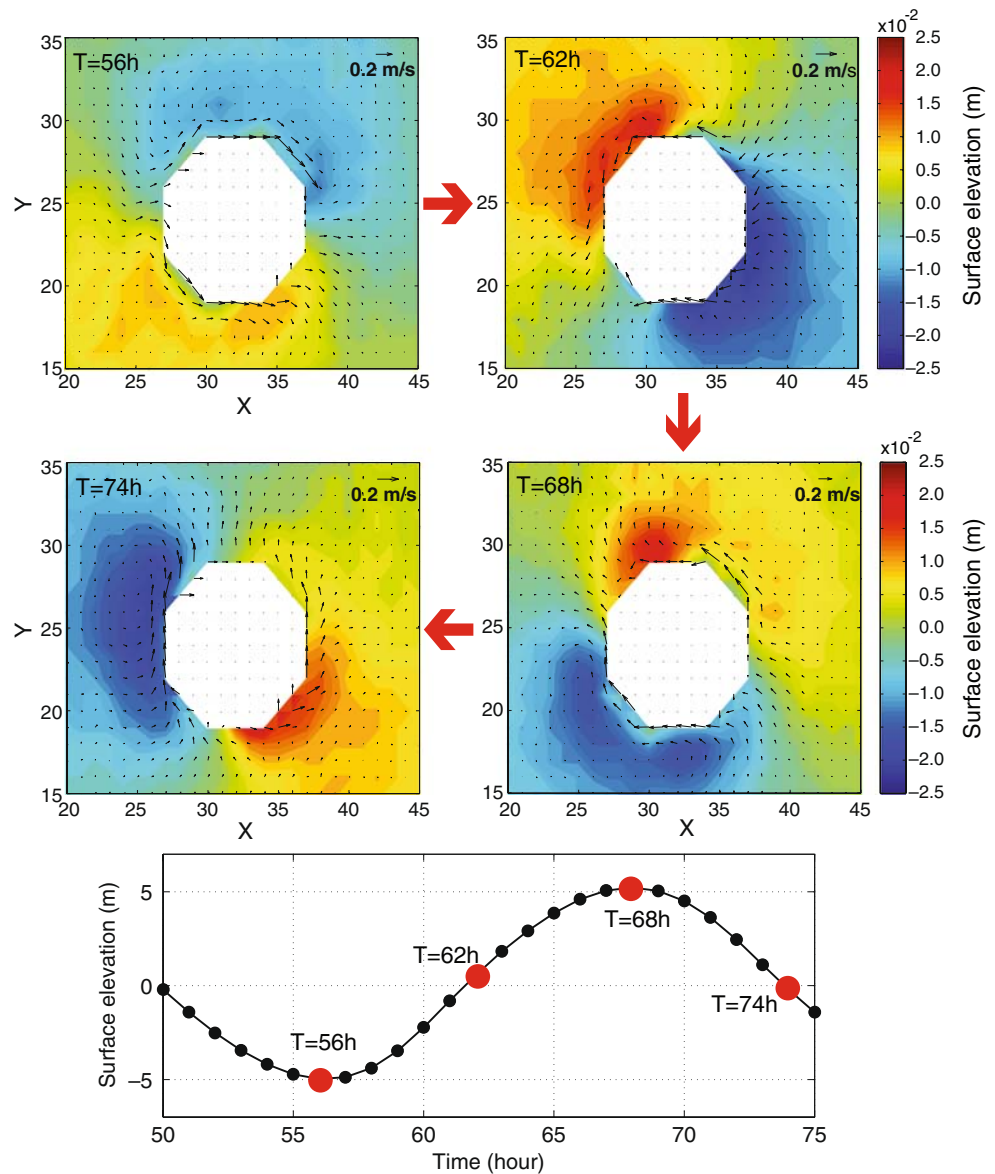
tides will propagate as gravity waves with speeds of $C = \sqrt{gH}$, where H is the depth. In our case, the average depths along line *a* and line *b* are approximately 12 and 50 m, respectively; therefore, the wave speeds for the coastal and large-scale domains are approximately 11 and 22 m s^{-1}, respectively. These values are consistent with the speeds calculated from the Hovmöller diagram, but only at the very beginning of the simulations (bottom panels of Fig. 4). However, after half a day, the speeds decrease from 11 to 2 m s^{-1} for the coastal waves and from 22 to 10 m s^{-1} for the large-scale waves. The explanation for this behavior is that, initially, the propagation is like free coastal waves, but later, the motion becomes dominated by the tidal period. The behavior of an idealized basin forced at an open end by

long waves with frequency $\omega = 2\pi/T$ depends on the factor $F = \omega L/C$, where T is the period of the forcing and L the length of the basin (e.g., see Fig. 9–12 in Mellor 1996). If $F = \pi/2$, the forcing creates a resonant with infinite amplitude (if friction is ignored). In our case, the tidal forcing has $T = 24$ h and $C = 22$ m s^{-1}, so $\omega = 7.2 \times 10^{-5}$ and $F = 1.14 = 0.74(\pi/2)$. Therefore, the motion is just under the resonant condition but apparently close enough so that the tidal forcing on the open boundary dominates the flow. If the imposed period of the waves is $T = 24$ h and the lengths of lines *a* and *b* are $X_a = 175$ km and $X_b = 915$ km, the expected propagation speeds are $C_a = X_a/T = 2.03$ m s^{-1} and $C_b = X_b/T = 10.59$ m s^{-1}, respectively; these values are almost exactly what we calculated from Fig. 4.
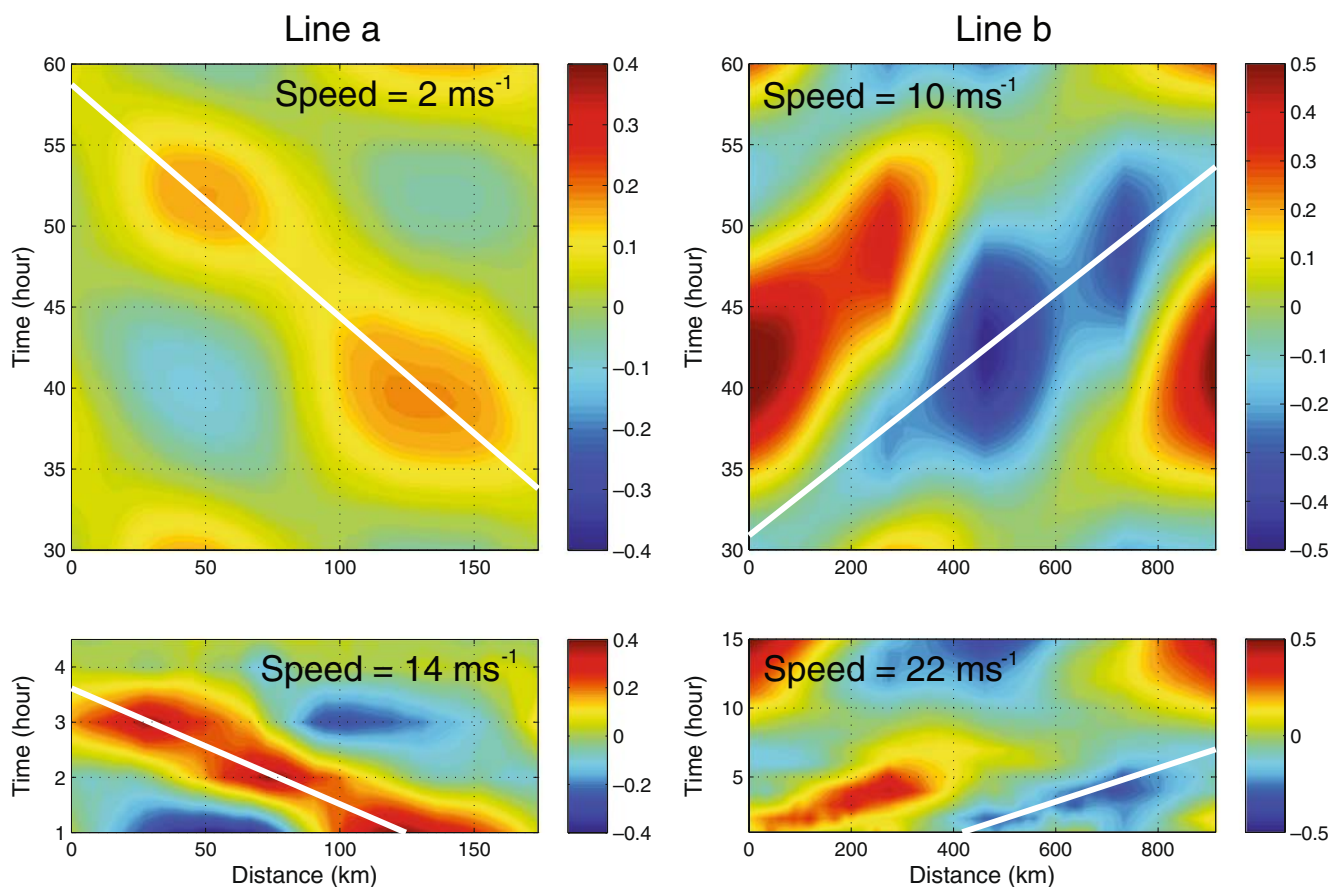
Fig. 4 Hovmöller diagram of surface elevation anomaly vs time (*y-axis*) and distance (*x-axis*) along line *a* ("coastal waves," *left panel*) and line *b* ("basin waves," *right panel*) for WAD TR1 case (see Fig. 1 for location of lines). The *lower panels* show the beginning of the simulation and the *top panels* show the results after more than 1 day. *Numbers* in each diagram represent the speed calculated from the slope of the *white lines*. Note that the distance and time axes are different in each *panel*

Two notes on the wave propagation are needed here. First, since the waves after the initial adjustment are dominated by the tidal period, the propagation speed for WAD and NoWAD are almost identical. Second, the open boundary condition on the eastern boundary allows these channel waves (see Fig. 10-7 in Mellor 1996), whereas eastward propagation along the southern boundary and westward propagation along the northern boundary combined for a counter-clockwise basin-scale wave. Based on the above analysis, we can now explain the impact of WAD as seen in Fig. 3. In our case, the propagation speed is not a function of depth (i.e., waves in the WAD and NoWAD cases propagate at similar speeds controlled by the tidal frequency), so the difference between WAD and NoWAD is the result of different wave amplitudes. The result is consistent with the simulation in Cook Inlet, Alaska (Oey et al. 2007), where the model tidal amplitudes were larger by ∼20% in WAD simulations compared to NoWAD simulations.

Note that the direction of signal propagation is still controlled by coastal wave dynamics with opposite propagation speed for the basin-scale and coastal waves so that the coast (in line *a*) or the model boundary (in line *b*) are to the right of the propagation direction; a geostrophic balance is maintained in the direction perpendicular to the boundary. Experiments (not shown) with a negative Coriolis parameter look similar to the results presented here, but the propagation of signals is in the opposite direction to that shown in Fig. 4. The experiment with no rotation (Coriolis parameter set to zero, experiment NC1 and NC4) has mostly east–west tidal flow with no clockwise or anticlockwise propagating waves.

Figure 5 shows the east–west u velocity and surface elevation across the center of the domain from south to north, comparing WAD, NoWAD, and zero Coriolis cases. Keep in mind that the flow is dominated by the tidal velocity, but also includes a constant eastward mean flow of 0.2 m s^{-1} and westward/eastward wind
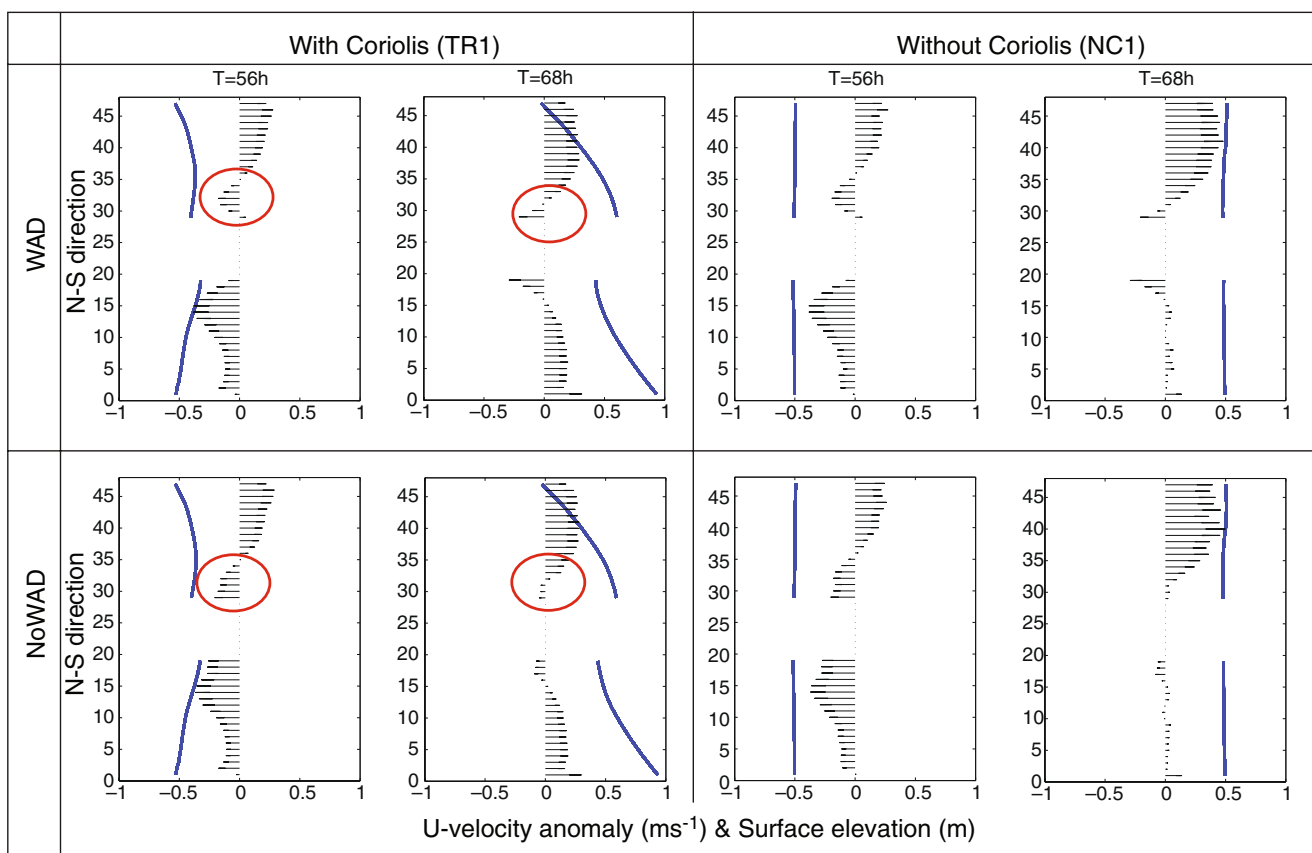
Fig. 5 North–south cross section (see Fig. 1) of u-velocity ("*stick diagram*" in m s^{-1}) and surface elevation (*blue lines* in m) at low tide: $T = 56$ h and high tide: $T = 68$ h for case TR1 and NC1. *Top* panels are for WAD cases and *bottom panels* are for NoWAD cases. The *red circles* highlight an area where horizontal velocity is affected by WAD

north/south of the island. In the case of no rotation, the surface elevation across the channel is flat as there is no geostrophic flow, so for example, in the right columns of Fig. 5, the only forcing during high tide is the mean flow plus the wind-driven part north of the island and the mean flow minus the wind-driven part south of the island (the two cancel each other to result in almost no flow). The impact of rotation is more pronounced during high tide (comparing the second and fourth columns) when surface elevation gradients (sloping blue lines in Fig. 5) are large and less pronounce during low tide (comparing the first and third columns). It is clearly seen that, close to the island, there is often a return flow in the direction opposite to the flow far from the center. Figure 5 also demonstrates the influence of WAD on the velocity shear near the island. During low tide, strong velocity shear near the island appears in the WAD case as flow slows down in the very shallow area near the island, while velocity remains high close to the (wall-like) boundary in the NoWAD case. During high tide, there are strong currents in the WAD case very close to the island as the water drains from the

flooded island; this is seen even in the case without rotation.

3.2 Mixing processes

The initial stratification is not space-dependent, so the evolution of the temperature structure is a good indication for mixing (mostly vertical mixing, horizontal mixing, and advection are much smaller). The temperature cross-sections at the center of the model domain along the east–west direction for small tide (TR1) and large tide (TR4) are shown in Fig. 6 (only for WAD case). It is clearly seen that, within 1 day, the temperature structure for case TR4 is totally destroyed, meanwhile the stratification still remains largely intact for case TR1, except very close to the island. Note the asymmetry with respect to the direction of the incoming tides, whereas larger temperature changes occur in front of the island (left-hand side), where tide is forced at the open boundary.

Figure 7 shows the vertical mixing coefficient calculated by the Mellor–Yamada turbulence scheme (in a
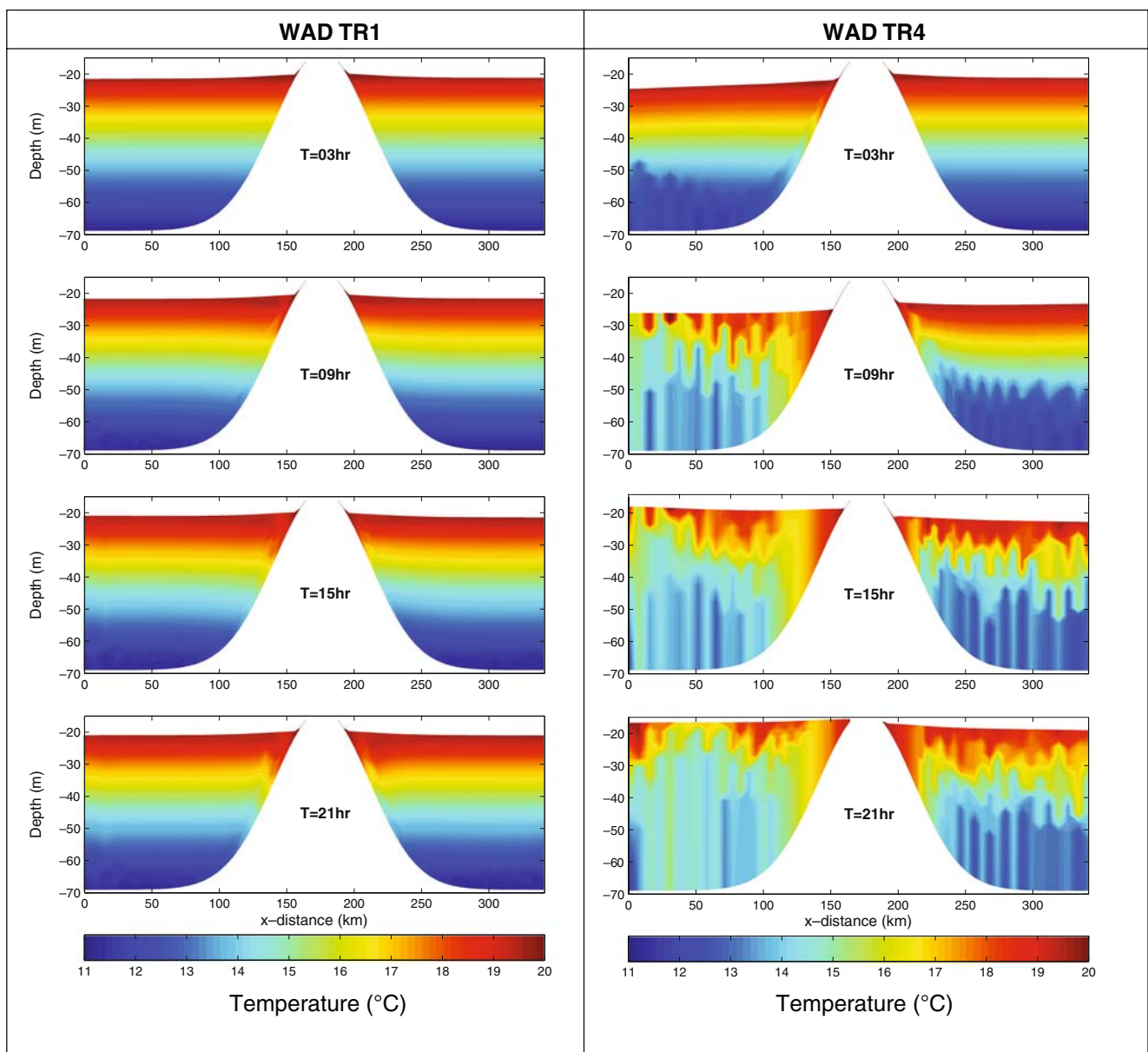
Fig. 6 East–west temperature cross sections (see Fig. 1) within one tidal cycle for WAD case (*left panels* are for small tides (TR1 case) and *right panels* are for large tides (TR4 case)

$\log_{10}(K_M)$ units) across the center of the model domain (east–west section), comparing cases TR1 and TR4 (WAD). The strong influence of the tidal amplitude on the mixing processes is clearly seen in the development of both the SML and the BBL. The strong tidal-induced bottom mixing in TR4 causes the SML and BBL to merge after ~9 h west of the island and after ~15 h east of the island. To demonstrate the impact of initial stratification on the mixing, Fig. 8 shows the mixing coefficient as in Fig. 7, but for experiments NS1 and NS4 (WAD cases without stratification). As expected, mixing coefficients are larger in homogeneous waters

compared with stably stratified waters. The east–west asymmetry in mixing still exists, but the thickness of the SML and BBL are more than twice those in the stratified case. The impact of stratification may be important for sediment transport modeling and other coastal processes that depend on mixing.

The time evolution of mixing ($\log_{10}(K_M)$) and temperature over ten tidal cycles, comparing four different tidal ranges (cases TR1, TR2, TR3, and TR4) at a deep-water location c (see Fig. 1), is illustrated in Fig. 9. The SML and BBL for the 1-m tidal range (case TR1) are still separated even after 10 days and the stratification
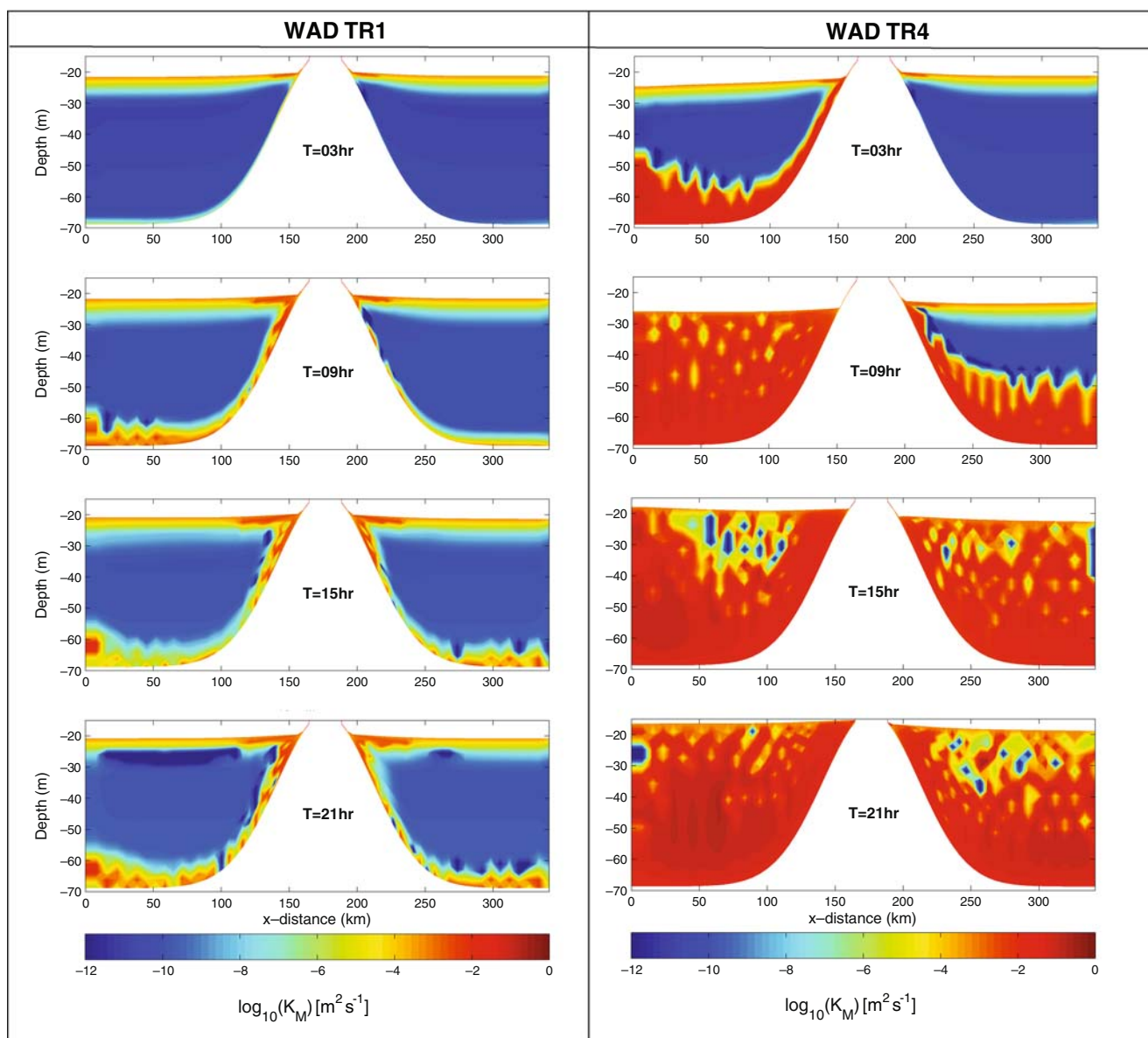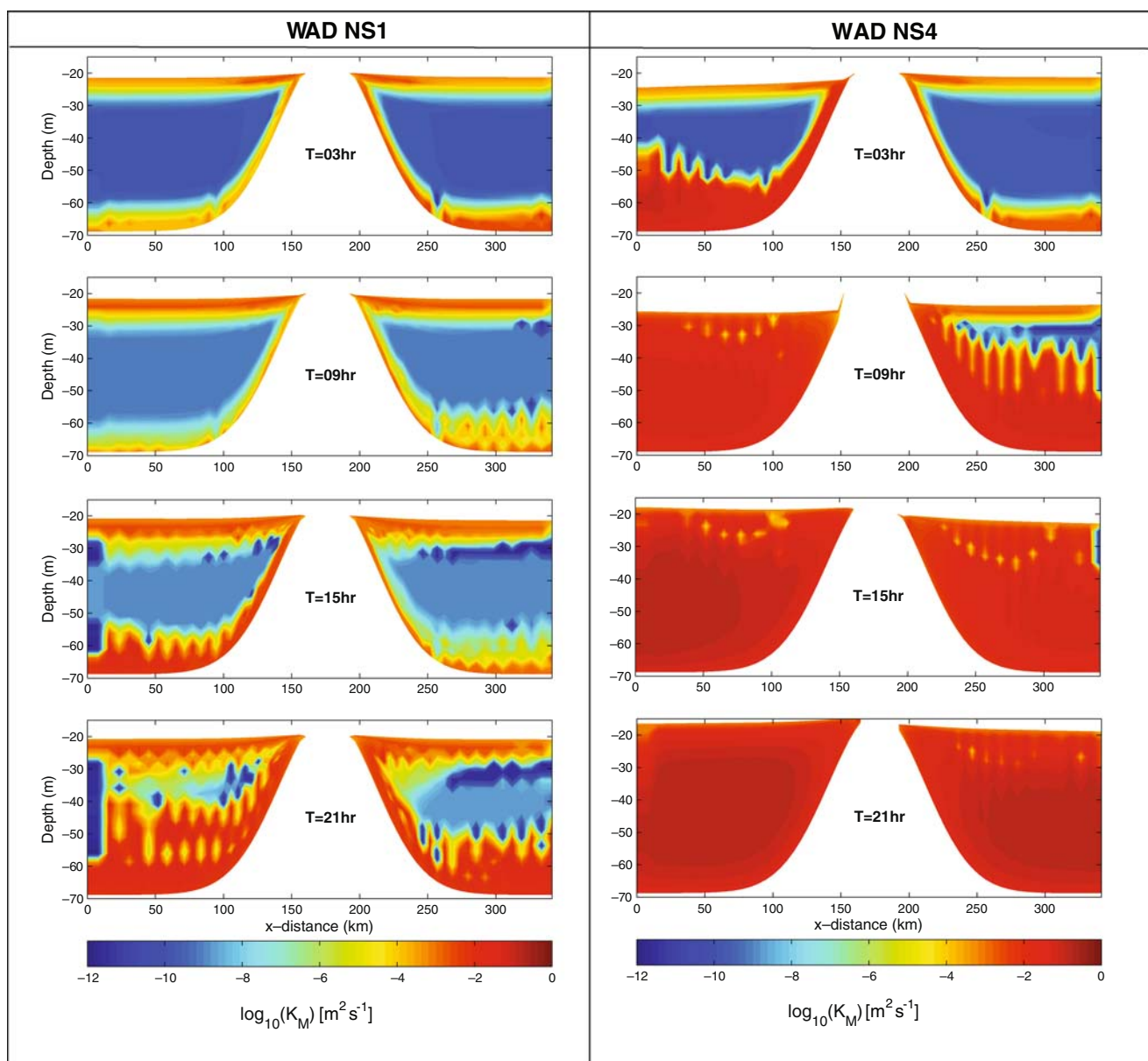
Fig. 7 Cross section as in Fig. 6, but for the mixing coefficient (in $\log_{10}(K_M)$ unit)

is well maintained, while for larger tides, the SML and BBL will merge at some point (after ∼1 day in TR4 and ∼8–10 days in TR3). An interesting result is that, for TR1 and TR2 cases, the thickness of SML tends to increase with time, causing the thermocline to *deepen*, while for TR3 and TR4, the thickness of BBL increases with time, resulting in the thermocline getting *shallower* with time. The explanation for this non-linear thermocline behavior with respect to tidal amplitude is that there is a threshold tipping point in which bottom mixing becomes dominant relative to wind-driven surface mixing. For the water depth of our experiments, surface wind-induced mixing dominates in TR1 and TR2 when tides are relatively small, but

tidal-induced bottom mixing dominate in TR3 and TR4 when tides are very large. To evaluate the role of the wind, experiments without wind forcing (NW1, NW2, NW3, and NW4) have been conducted and shown in Fig. 10. With no wind (and thus only tidal mixing), there is no SML and the stratification in the upper layer remains almost unaffected for small tides (cases NW1 and NW2). For larger tides (cases NW3 and NW4), which are dominated by tidal-driven BBL mixing, the results are similar to the cases with wind (comparing the bottom two panels in Figs. 9 and 10).

We have seen that the inclusion of WAD in the model may affect coastal waves (Fig. 3) and near-coast velocities (Fig. 5), but how does WAD affect mixing

Fig. 8 Mixing coefficient cross section as in Fig. 7, but for the cases without stratification (*left/right panels* for: NS1/NS4 cases, respectively)

processes? Figure 11 compares the K_M profiles at location *d* (case TR1) for WAD and NoWAD. The surface mixing, which is dominated by wind in this case, is not significantly affected by WAD, so mixing coefficients in the top 5 m are almost the same in the WAD and NoWAD cases. However, in deeper layers, the difference between WAD and NoWAD is large, whereas the NoWAD case generally shows larger mixing than the WAD case. During low tide ($T = 57$ h), the difference between WAD and NoWAD is more pronounced near the bottom, while during high tide ($T = 69$ h), the difference is more pronounced in middle depths. The region of low mixing between the SML and the BBL

(at the thermocline depth) seems to be deeper by 2–4 m in the NoWAD case than in the WAD case. As seen from the horizontal velocities (Fig. 5), during low tide, the absorption of energy by the shallow water column in the WAD case (compared with the 10-m minimum depth in the NoWAD case) results in weaker currents and less near-bottom mixing near the coast. Close examination of the interaction of the tides with the coastal boundary suggests that additional mixing in the NoWAD case may result from more reflection of waves from the vertical wall compared with more absorption of energy when waters are allowed to flow up the slope if WAD is included in the model. The
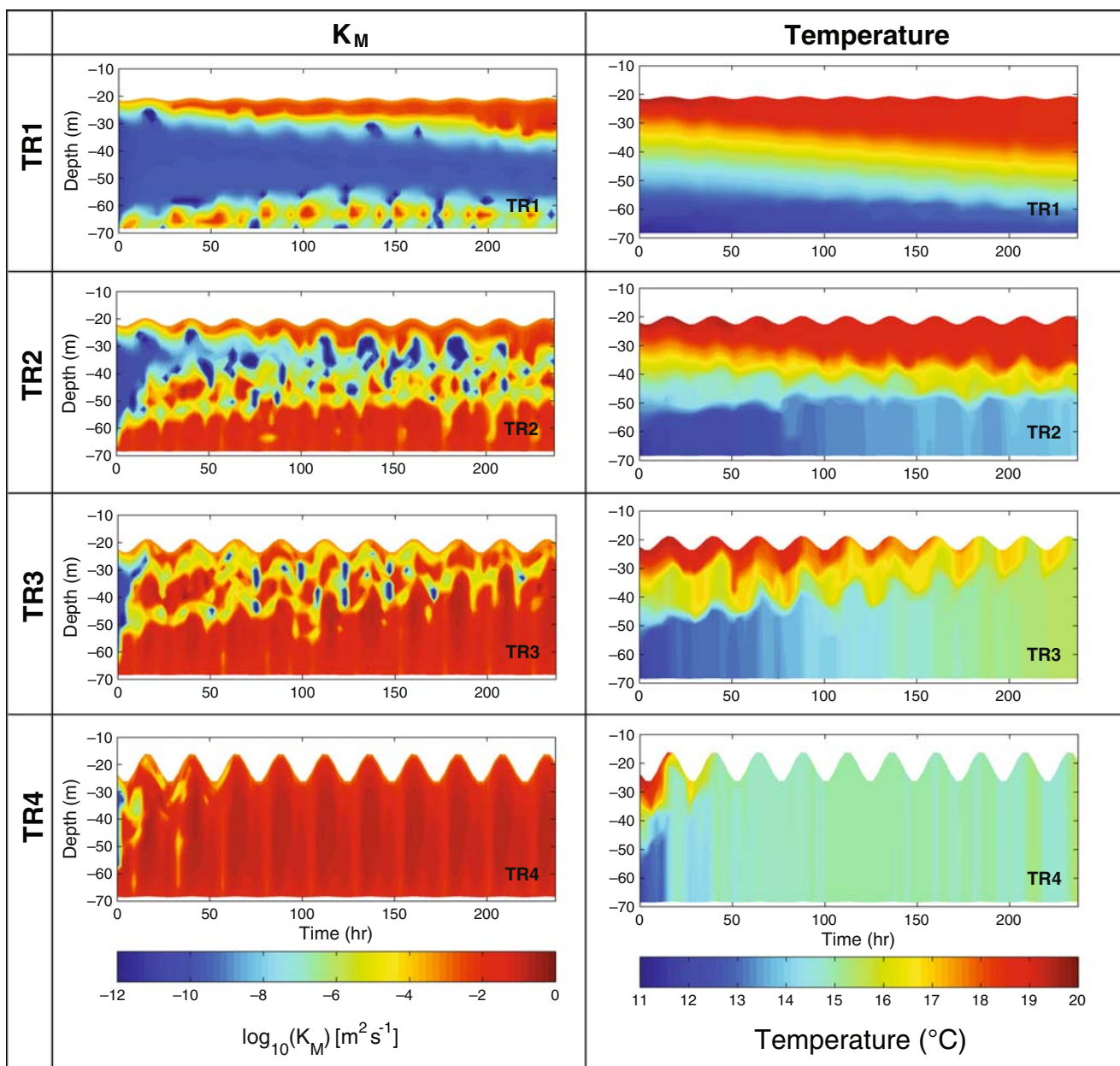
Fig. 9 Time evolution of $\log_{10}(K_M)$ (*left panels*) and temperature (*right panels*) for WAD case at location c (see Fig. 1) for four different tidal ranges: 1.00 m (TR1), 2.75 m (TR2), 4.50 m (TR3), and 9.00 m (TR4), from *top* to *bottom*

implication of this result might be important for studies of coastal morphology dynamics and sediment transport simulations.

3.3 Momentum balance

To further evaluate the dynamics of the flow and compare the various experiments presented here, the momentum terms in the vertically integrated vorticity balance Eq. 1 across the center of the model domain are calculated during flood and ebb for the different experiments (Figs. 12 and 13). Generally, the three largest terms are the surface elevation gradient, the bottom stress, and the tendency terms; advection may play a minor role in some cases. The surface stress, the JEBAR, and the Coriolis terms are much smaller in these simulations. The bottom stress changes sign some distance from the coast because the coastal return flow around the island is in a direction opposite to the large-scale tidal flow around the whole domain (Fig. 5). Note also the asymmetry between flood and ebb, with all terms larger during flood (left panels of Figs. 12 and 13)
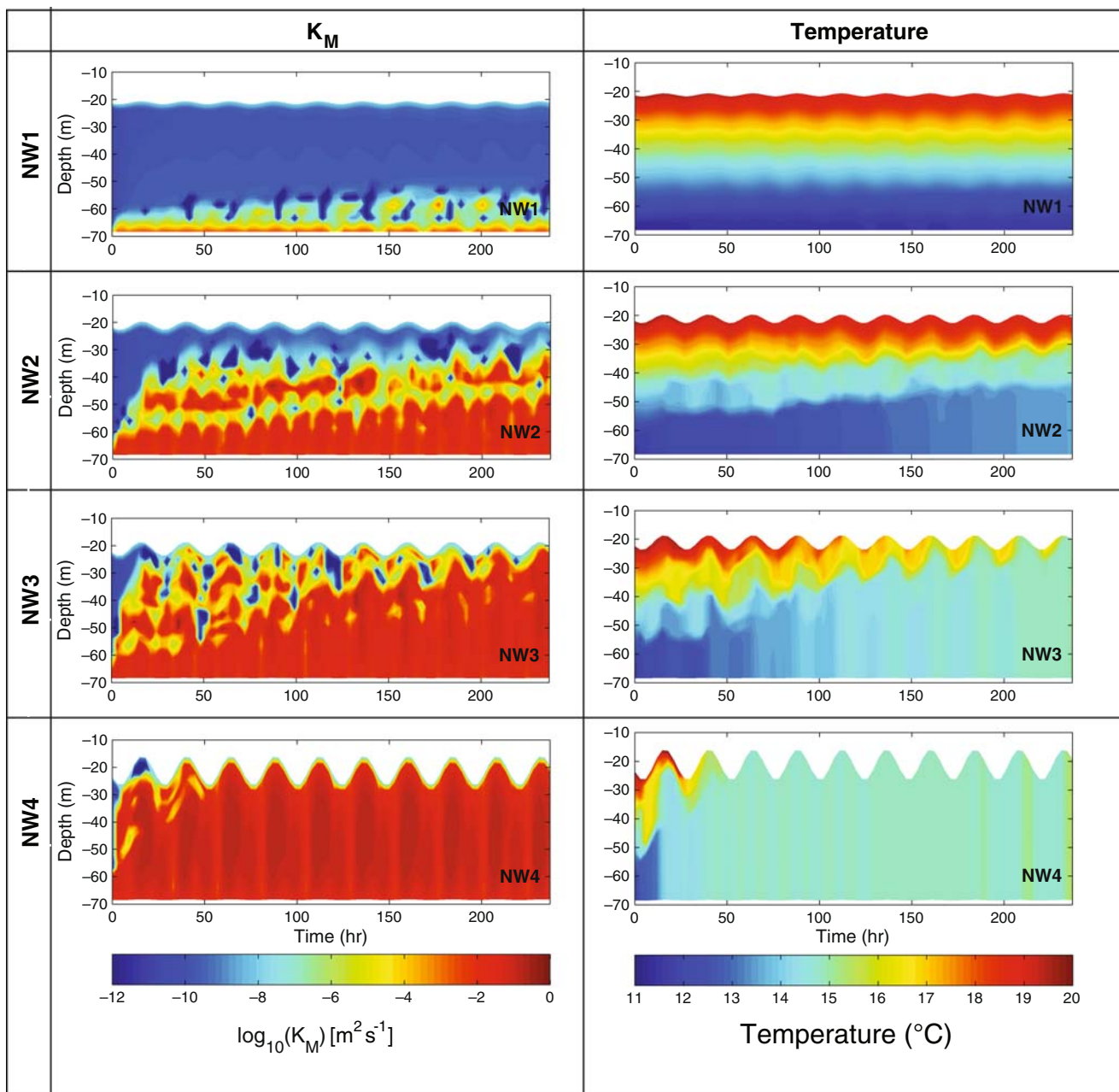
Fig. 10 Same as Fig. 9, but for the cases without wind (NW1–NW4)

than during ebb (right panels of Figs. 12 and 13). Below is the summary of the impact of the various parameters tested.

Impact of WAD Figure 12 compares the dynamics of WAD and NoWAD cases for small tide (TR1, top two panels) and large tide (TR4, bottom two panels). Within ~30 km from the island, the magnitude of the bottom stress in the WAD case is approximately two times larger than that of the NoWAD case, causing the surface elevation gradient term to be more important

as it needs to balance the bottom stress. With large tides, there are only three dominant terms where the time-dependent flow (tendency term) is driven by the balance between the surface slope and bottom stress. However, for small tides, the terms are noisier, as additional terms like advection start to play a role. To evaluate the other parameters below, only experiments with small tides are shown in Fig. 13.

Impact of wind In our experiments, the direct impact of the wind through the surface stress is small compared
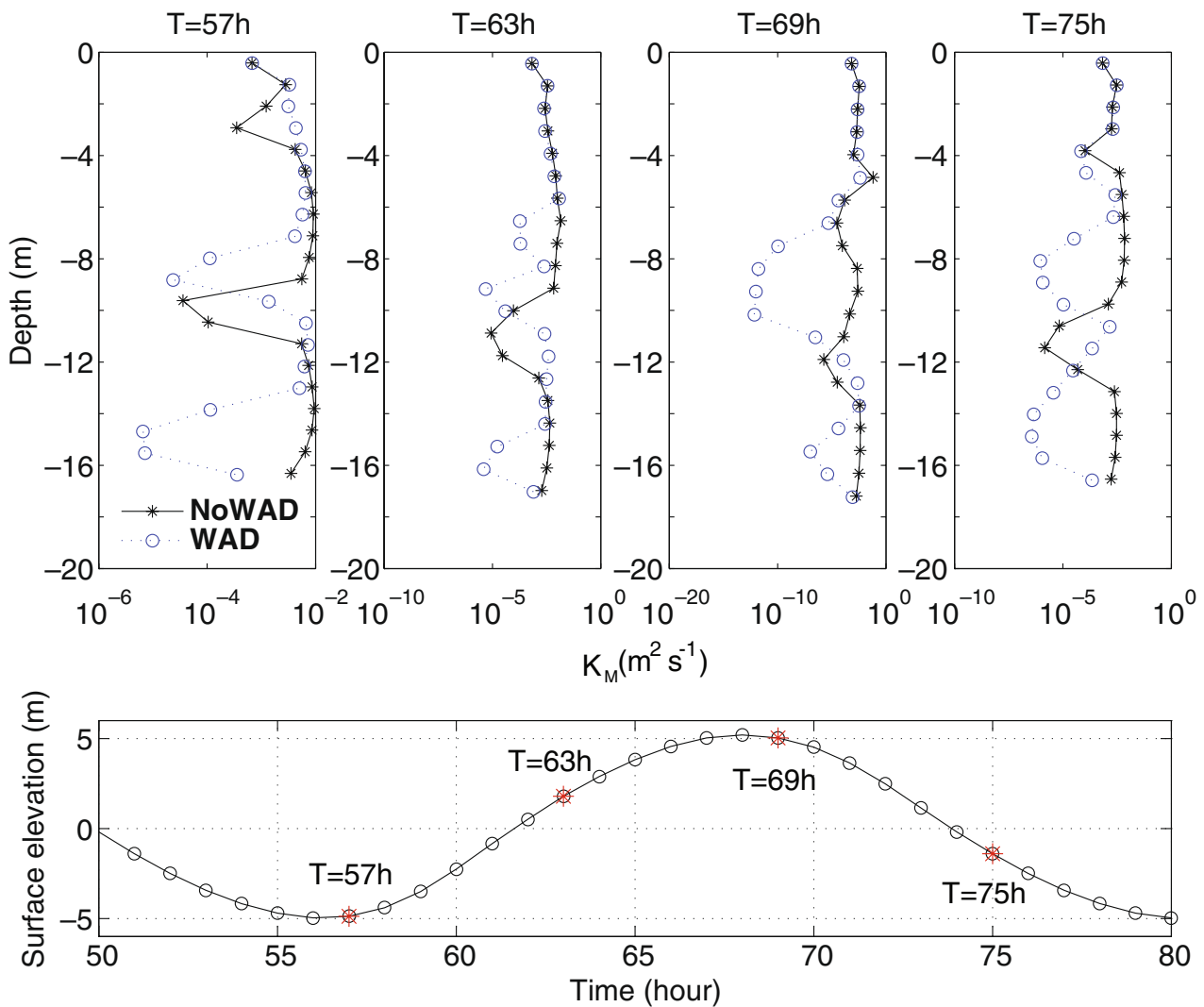
Fig. 11 *Top panel*: K_M profiles at location d (see Fig. 1) for TR1 case: *solid-asterisk lines* are for NoWAD and *dash-circle lines* are for WAD cases. *Lower panel*: Surface elevation at that location, with *red stars* indicating the time of the four *top panels*. Note that the x-axis for K_M profile is represented in a logarithmic scale with different range for each time

to the other terms (second panels from the top in Fig. 13). However, wind affects the dynamics indirectly by changing the stratification and, thus, the baroclinic pressure gradient and advection, so the tendency and the advection terms are different in NW1 compared with the control run TR1. Wind stress also plays an important role for the evolution of the SML (Figs. 9 and 10) through wind-driven mixing, but less so for the vorticity evolution (Figs. 12 and 13).

Impact of stratification Without stratification (case NS1, third panels from the top in Fig. 13), the bottom stress, tendency, and advection terms are generally smaller and much smoother than in the control case (TR1). The reason is that the tidal mixing creates spatial (Fig. 6) and temporal (Fig. 9) variations in tempe-

rature that induce variations in the baroclinic pressure gradients and associated variations in velocities.

Impact of rotation Without Coriolis (case NC1, bottom panels in Fig. 13), there is no geostrophic balance, so terms other than Coriolis have to balance the pressure gradient in the interior and friction in the SML and the BBL (no Ekman boundary layer balance). The result is much noisier and more spatially dependent changes in the advection, bottom stress, and tendency terms. Note that the surface gradient term is not zero, due to the large contribution from the along-channel slopes driven by the tidal forcing. This case may apply to inundation processes in low-latitude regions.
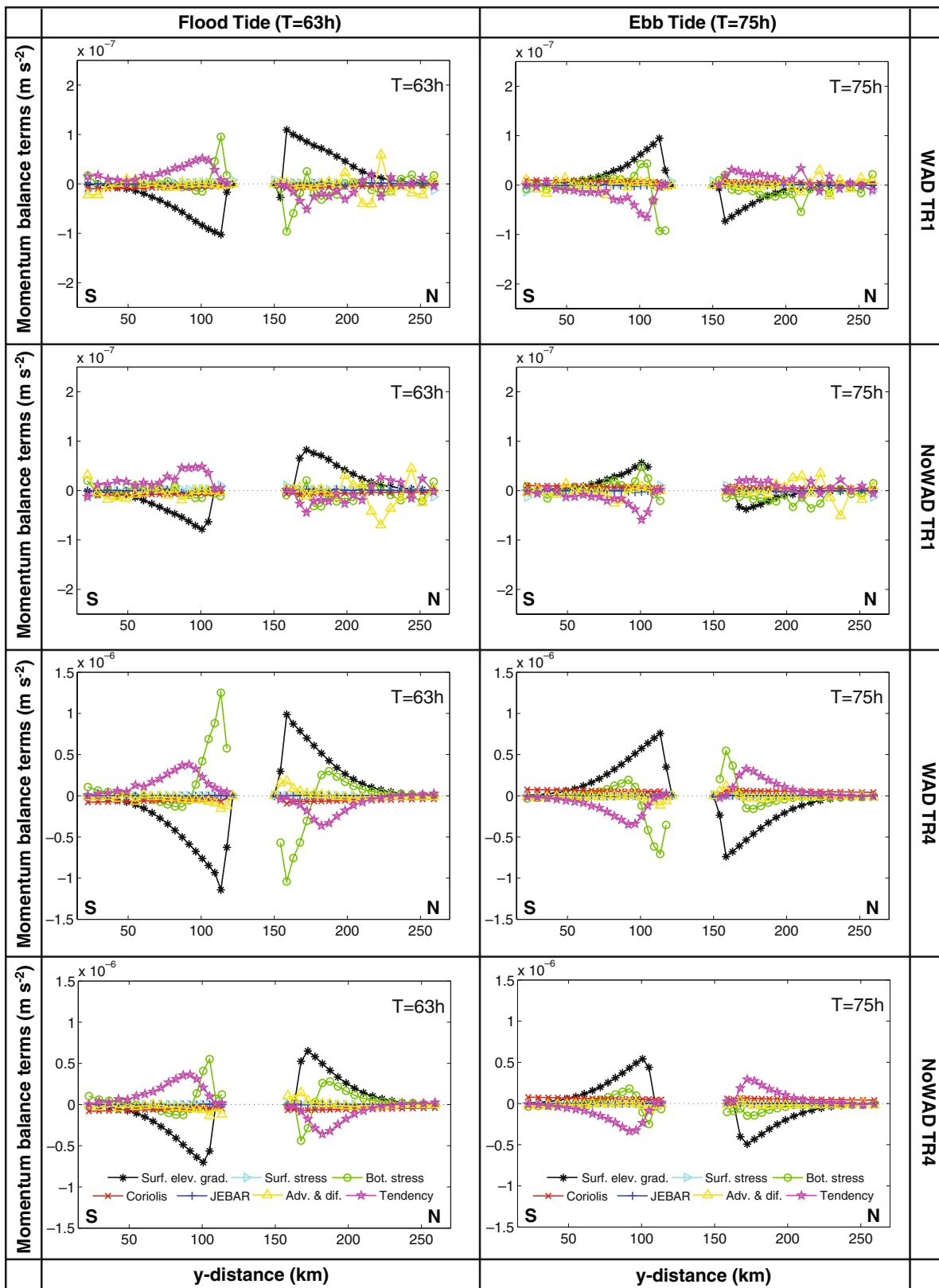
Fig. 12 North–south cross section (see Fig. 1) of the momentum balance terms in unit of m s^{-2} for small tides (WAD TR1 and NoWAD TR1 in the *top two panels*) and for large tides (WAD TR4 and NoWAD TR4 in the *bottom two panels*). *Left* and *right panels* are for flood ($T = 63$ h) and ebb ($T = 75$ h) tides, respectively
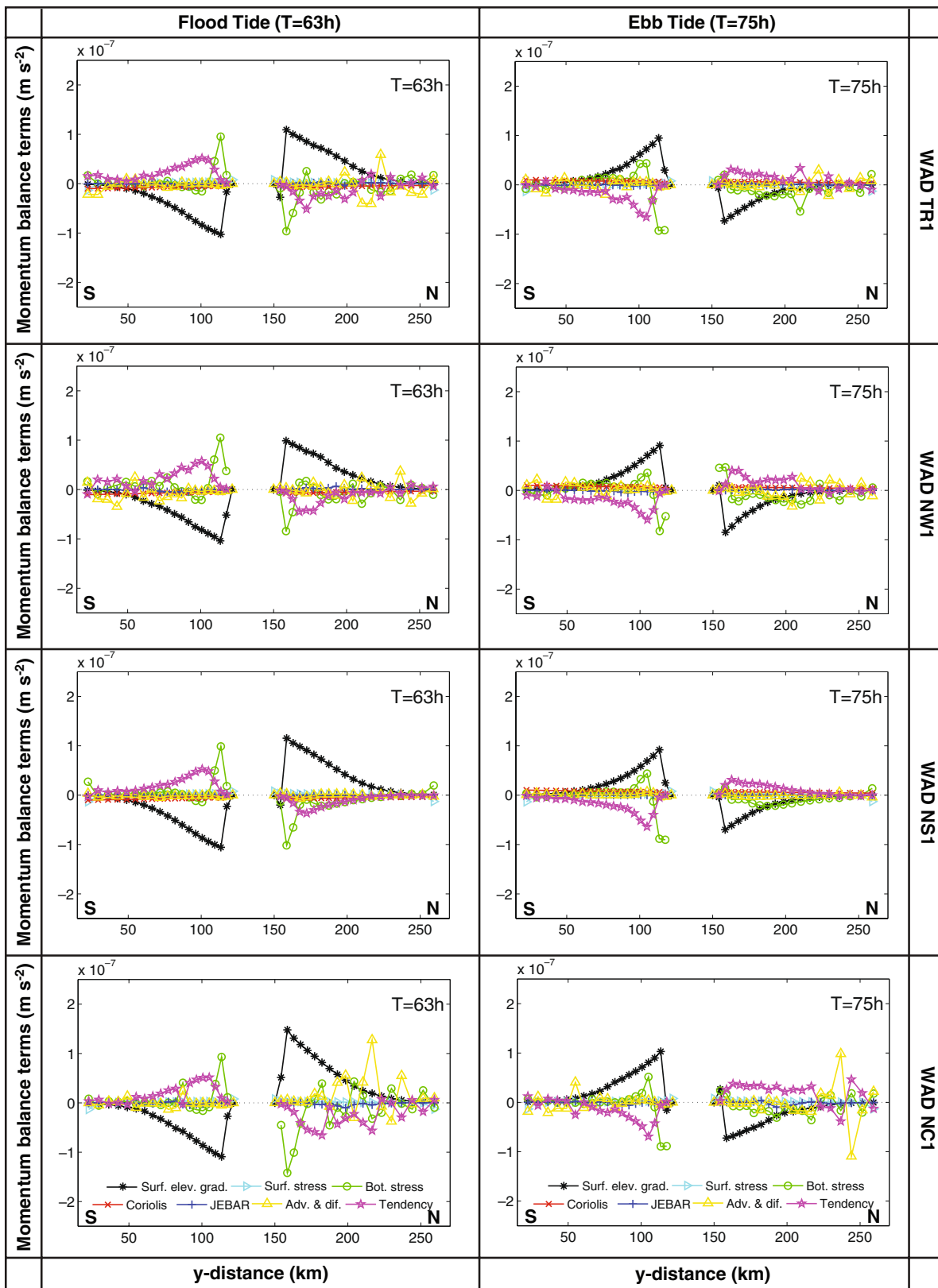
Fig. 13 Same as Fig. 12, but for different experiments with WAD, from *top* to *bottom*: control case (TR1, identical to *top panel* of Fig. 12), no-wind case (NW1), no-stratification case (NS1) and no-Coriolis case (NC1)

4 Summary and conclusions

Comprehensive sensitivity experiments (∼30 different runs) with a newly developed WAD scheme, WAD-POM, implemented in a widely used three-dimensional community ocean circulation model (Oey 2005, 2006; Oey et al. 2007; Ezer et al. 2008; Ezer and Liu 2009), have been conducted in order to study tidal-driven mixing processes in the coastal environment. Model calculations are compared with a control model without the WAD scheme. In this study, an idealized configuration with an emerged seamount (island) at the center of the model domain is implemented. In addition to the impact of WAD, other parameters tested include grid size, tidal amplitude, wind, stratification, and rotation. To investigate wave propagation and velocity field with the stratified water near the island, model results with three different grid sizes are compared. The simulations show an asymmetric flow with large-scale counter-clockwise propagating tidal waves along the boundary, but clockwise propagating topographic waves around the island. The wave propagation speeds are initially consistent with the theoretical barotropic gravity wave speeds, but within a day or so become dominated by the tidal frequency, resulting in slower wave speeds. The WAD impacts the amplitude of the coastal waves in an uneven way with amplitudes larger than NoWAD in the side of the island facing the incoming tide, and vice versa on the other side of the island, resulting in time-dependent discrepancy between WAD and NoWAD simulations (Fig. 3), not just a predictable bias that can be corrected analytically in coastal models without WAD.

For small tides (less than 3-m range) the wind-induced mixing dominates, impacting the SML, while for large tides (up to 9-m range), tidal-induced mixing dominates, impacting the BBL. Therefore, the evolution of the thickness of the SML and BBL with time is controlled by the balance between wind forcing and tidal forcing, resulting in thermocline deepening for small tides and thermocline shallowing for large tides. For large enough tides, the SML and BBL merge and a complete top-to-bottom mixing occurs. Near the coast, the boundary in a NoWAD case (and in most general ocean circulation models) is an artificial vertical sea-wall, while in a WAD case, the energy is absorbed by the land–water interaction. Vertical mixing coefficients (calculated by the Mellor–Yamada turbulence scheme) are thus affected by inclusion of WAD, through the changes in bottom stress and velocity shear resulted from the inundation dynamics.

Evaluation of the momentum balance in the model shows that the surface elevation gradient, the bottom stress, and the tendency terms are the dominant terms in tidal simulation, while surface stress, advection, and Coriolis terms are less important. There is little difference between WAD and NoWAD at the deeper part away from the coast, especially for large tides, but within ∼30 km from the coast, simulations with WAD show twice as large contribution from bottom stress and surface elevation gradient terms compared with a NoWAD case. The results presented here provide a preliminary evaluation of the model with an idealized configuration, demonstrating the complex way in which WAD may affect coastal ocean simulations under different conditions and wide ranges of parameters. More experiments with different topographies and realistic configurations and forcing are clearly needed and will follow in future studies.

References

Beckmann A, Haidvogel DB (1993) Numerical simulation of flow around a tall isolated seamount. Part I: problem formulation and model accuracy. J Phys Oceanogr 23(8):1736–1753

Chen C, Huang H, Beardsley RC, Liu H, Xu Q (2007) A finite volume numerical approach for coastal ocean circulation studies: comparisons with finite difference models. J Geophys Res 112:C03018. doi:10.1029/2006JC003485

Ezer T, Liu H (2009) Combining remote sensing data and an inundation model to map tidal mudflat regions and improve flood predictions: a proof of concept demonstration in Cook Inlet, Alaska. Geophys Res Lett 36:L04605. doi:10.1029/2008GL036873

Ezer T, Mellor GL (1994) Diagnostic and prognostic calculations of the North Atlantic circulation and sea level using a sigma coordinate ocean model. J Geophys Res 99(C7):14159–14171

Ezer T, Mellor GL (2000) Sensitivity studies with the North Atlantic sigma coordinate Princeton Ocean Model. Dyn Atmos Ocean 32:185–208

Ezer T, Arango H, Shchepetkin A (2002) Developments in terrain-following ocean models: intercomparisons of numerical aspects. Ocean Model 4(3-4):249–267

Ezer T, Hobbs R, Oey LY (2008) On the movement of Beluga whales in Cook Inlet, Alaska: simulation of tidal and environment impacts using a hydrodynamic inundation model. Oceanography 21(4):186–195

Heniche M, Secretan Y, Boudreau P, Leclerc M (2000) A two-dimensional finite element drying-wetting shallow water model for rivers and estuaries. Adv Water Resour 23(4):359–372. doi:10.1016/S0309-1708(99)00031-7

Ioualalen M, Asavanant J, Kaewbanjak N, Kirby ST, Watts P (2007) Modeling the 26 December Indian Ocean tsunami: case study of impact in Thailand. J Geophys Res 112:C07024. doi:10.1029/2006JC003850

Jiang YW, Wai OWH (2005) Drying-wetting approach for 3d finite element sigma coordinate model for estuaries with large tidal flats. Adv Water Resour 28(8):779–792. doi:10.1016/j.advwaters.2005.02.004

Kamiya M, Hiramatsu K, Harada M, Mori M (2006) A three-dimensional sigma-coordinate ocean model with a wetting and drying scheme and its application to Isahaya Bay. Sci Bull Fac Agr, Kyushu Univ 61(2):289–296

Mellor GL (1996) Introduction to physical oceanography. American Institute of Physics, Woodbury, p 260

Mellor GL (2004) User's guide for a three-dimensional, primitive equation, numerical ocean model. Program in atmospheric and oceanic sciences. Princeton University, Princeton, p 56

Mellor GL, Yamada T (1982) Development of a turbulent closure model for geophysical fluid problems. Rev Geophys 20:851–875

Mellor GL, Oey LY, Ezer T (1998) Sigma coordinate pressure gradient errors and the seamount problem. J Atmos Ocean Technol 15:1122–1131

Oey LY (2005) A wetting and drying scheme for POM. Ocean Model 9(2):133–150. doi:10.1016/j.ocemod.2004.06.002

Oey LY (2006) An OGCM with movable land-sea boundaries. Ocean Model 13(2):176–195. doi:10.1016/j.ocemod.2006.01.001

Oey LY, Ezer T, Hu C, Muller-Karger FE (2007) Baroclinic tidal flows and inundation processes in Cook Inlet, Alaska: numerical modeling and satellite observations. Ocean Dyn 57(3):205–221. doi:10.1007/s10236-007-0103-8

Sobey RJ (2009) Wetting and drying in coastal flows. Coast Eng 56(5–6):565–576. doi:10.1016/j.coastaleng.2008.12.001

Uchiyama Y (2004) Modeling wetting and drying scheme based on an extended logarithmic law for a three-dimensional sigma-coordinate coastal ocean model. Rep Port Airport Res Inst 43(4):3–21

Westerink JJ, Luettich RA, Feyen JC, Atkinson JH, Dawson C, Roberts HJ, Powell MD, Dunion JP, Kubatko EJ, Pourtaheri H (2008) A basin to channel scale unstructured grid hurricane storm surge model applied to southern Louisiana. Mon Weather Rev 136(3):833–864

Xie L, Pietrafesa LJ, Peng M (2004) Incorporation of a mass-conserving inundation scheme into a three-dimensional storm surge model. J Coast Res 20:282–296